Fluid-Structure Interaction and multi-body contact. Application to the aortic valves

Matteo Astorino, Jean-Frédéric Gerbeau, Olivier Pantz, Karim-Frédéric Traore

INRIA

INSTITUT NATIONAL DE RECHERCHE EN INFORMATIQUE ET EN AUTOMATIQUE

Fluid-structure interaction and multi-body contact. Application to aortic valves

Matteo Astorino — Jean-Frédéric Gerbeau — Olivier Pantz — Karim-Frédéric Traoré

N° 6583

July 2008

Thème BIO

ISSN 0249-6399 ISRN INRIA/RR--6583--FR+ENG

INSTITUT NATIONAL
DE RECHERCHE
EN INFORMATIQUE
ET EN AUTOMATIQUE

INRIA

centre de recherche
PARIS - ROCQUENCOURT

Fluid-structure interaction and multi-body contact. Application to aortic valves

Matteo Astorino*, Jean-Frédéric Gerbeau†, Olivier Pantz‡, Karim-Frédéric Traoré§

Thème BIO — Systèmes biologiques
Équipes-Projets REO

Rapport de recherche n° 6583 — July 2008 — 23 pages

Abstract: We present a partitioned procedure for fluid-structure interaction problems in which contacts among different deformable bodies can occur. A typical situation is the movement of a thin valve (*e.g.* the aortic valve) immersed in an incompressible viscous fluid (*e.g.* the blood). In the proposed strategy the fluid and structure solvers are considered as independent "black-boxes" that exchange forces and displacements; the structure solvers are moreover not supposed to manage contact by themselves. The hypothesis of non-penetration among solid objects defines a non-convex optimization problem. To solve the latter, we use an internal approximation algorithm that is able to directly handle the cases of thin structures and self-contacts. A numerical simulation on an idealized aortic valve is finally realized with the aim of illustrating the proposed scheme.

Key-words: fluid-structure interaction, contact, cardiac valves

* Project-team REO, INRIA Paris-Rocquencourt
† Project-team REO, INRIA Paris-Rocquencourt
‡ CMAP, Ecole Polytechnique
§ Project-team REO, INRIA Paris-Rocquencourt

Centre de recherche INRIA Paris – Rocquencourt
Domaine de Voluceau, Rocquencourt, BP 105, 78153 Le Chesnay Cedex
Téléphone : +33 1 39 63 55 11 — Télécopie : +33 1 39 63 53 30

Interaction fluide-structure et contact multi-solides. Application aux valves aortiques

Résumé : Nous présentons un algorithme de couplage partitionné pour des problèmes d'interaction fluide-structure dans lesquels des contacts peuvent se produire entre plusieurs solides élastiques immergés. La méthode s'applique par exemple aux valves aortiques (qui sont constituées de trois valvules baignées dans un fluide visqueux incompressible). La stratégie proposée considère les solveurs fluide et structure comme des "boites noires" indépendantes. De plus, le solveurs structure n'est pas supposé savoir gérer le contact. La contrainte de non pénétration entre les solides n'est pas convexe. Le problème est résolu de manière itérative en considérant une suite de problèmes avec contrainte convexe. L'algorithme, qui est capable de traiter l'autocontact et les structures minces, est illustré sur une configuration idéalisée de valves aortiques.

Mots-clés : interaction fluide-structure, contact, valves cardiaques

1 Introduction

We are interested in the interaction of several elastic bodies immersed in an incompressible viscous fluid. Cardiac valves are the main motivation of the present study, but our algorithms can address more general configurations.

The numerical simulation of cardiac valves offers many challenges: the constitutive laws of the valves are very complex, the blood interacts with the valves and the wall, the valves are submitted to kinematic constraints like contact between leaflets or attachments to the *chordae tendineae* (for the mitral valves). In this paper we are interested in the management of fluid-structure interaction in presence of contacts. More precisely, we propose a general strategy to address this problem with existing fluid and structure solvers, assuming that the structure solvers do not include contact capabilities.

The mechanical properties of the valve is an important topic which is beyond the scope of the present study. Different approaches have been proposed in literature. We refer to [1] for an overview of different constitutive models. For example, the fiber-reinforcement of the leaflets has been modeled as two layers of fibers in [2]. Recently, a multiscale approach, including cells, tissue and organ models, has been proposed in [3].

A number of articles has been devoted to fluid-structure interaction around artificial or natural cardiac valves. They can be roughly divided in three groups: the approaches based on the Immersed Boundary (IB) methods (see in particular [4] and the references therein), those based on the Arbitrary Lagrangian Eulerian (ALE) formulation (see *e.g.* [5, 6]), and those based on Fictitious Domains (FD) formulations (see *e.g.* [7, 8, 9, 10]). The present paper belongs to the third group.

The most common approach in mechanical contacts is known as the master/slave formulation (see [11], [12] and [13]). Initially designed to prevent a deformable body (the slave) to penetrate a rigid foundation (the master), it has been extended to the case of contacts between different deformable bodies. In this article, we consider the more complicated case of contacts and self-contacts between deformable thin structures. The master/slave approach can be adapted to this case (see [14]), though it is no more completely consistent from a mathematical viewpoint. *Ad hoc* modifications have therefore to be added in order to correctly handle the inconsistent situations in which the standard master/slave approach may fail. In this article, we propose to follow a totally different path, which allows us to consider contact, self-contact between thin or not thin structures in a single setting. For more details about the state of the art in contact mechanics, the reader is referred to [15], which contains many references, and to the monographs [16] or [17] (see also [18, 19]).

A few works have considered both fluid-structure interaction and the contact problem between the leaflets. For example, in [20], contact is taken into account with a rigid wall (convex constraint) and the algorithm is monolithic: fluid, structure and contact are governed by a unique *ad hoc* solver. In [10], the same kind of "simple" contact has been investigated but with a partitioned algorithm. In [21], the contact is handled directly in the structure solver. In [22], the "SENCT" contact algorithm has been introduced to preserve the quality of the fluid mesh between the structural surfaces coming into contact. Compared to the existing studies, the main characteristics of the present work are the following: (i) the solvers are kept independent; (ii) the structure solvers are

not supposed to manage contact by themselves; (iii) the contact occurs between several leaflets (non-convex constraint), which can be thin structures; (iv) self-contact is automatically managed.

In Section 2, we briefly present the models and their discretizations. The fluid is governed by the incompressible Navier-Stokes equations. The solids are modeled by nonlinear shell elements. The fluid and solid meshes are independent: the continuity of the fluid and solids velocities is imposed through Lagrange multipliers (FD formulation).

In Section 3, we present the general algorithm. The fluid-structure coupling is handled with a standard fixed-point accelerated by an Aitken extrapolation. The constraint of non-penetration among the immersed structures defines a non-convex optimization problem which is solved following an algorithm proposed in [23]. This approach is in particular able to manage the cases of thin structures and self-contacts. The proposed strategy allows to consider the fluid and structure solvers as "black-boxes" which only exchanges forces and displacements.

In Section 4, the algorithm is applied to the simulation of an idealized aortic valve. The proposed test case is far from the complexity of the real problem. Several simplifications should be relaxed to address the problem with more realism. In particular the constitutive laws should be improved and the elasticity of the aorta should be taken into account. The purpose is only to illustrate the algorithm in a configuration which is not trivial, in spite of all the simplifications.

2 Modeling and discretization

2.1 Fluid model

The fluid is governed by the incompressible Navier-Stokes equations. The approximation is performed with the finite element method. The structure and the fluid meshes are independent. The continuity of the displacement of the fluid and the structures is enforced through Lagrange multipliers, as it was proposed for example in [7]. We refer to [10] for the details of our approach.

2.2 Solid model

In view of the ratio thickness/size of the leaflets, it is necessary to consider robust structural models in order to avoid the well-known locking phenomena (see [24]). In this study we consider the MITC4 general shell element. This element is known to be reliable and effective in the two asymptotic states (membrane and bending) [25, 24] and can handle large displacements.

For the sake of simplicity, we use a generalized Hook law. It cannot be considered as a good model for biological valves. It is nevertheless sufficient to illustrate our algorithms. The internal stored energy $\mathcal{W}$ in the reference configuration of the solids $\hat{\Omega}_s$ is given by :

$$\mathcal{W} = \frac{1}{2} \int_{\hat{\Omega}_S} \left[C^{\alpha\beta\lambda\mu} e_{\alpha\beta} e_{\lambda\mu} + D^{\alpha\lambda} e_{\alpha z} e_{\lambda z} \right] dV, \tag{1}$$

where $\boldsymbol{e} = (e_{\alpha\beta})$ denotes the nonlinear Green-Lagrange strain tensor. In equation (1) the Greek symbols varying from 1 to 2 are used for the tangential

components to the surface, z is the third direction, and

$$C^{\alpha\beta\lambda\mu} = \frac{E}{2(1+\nu)}\left(g^{\alpha\lambda}g^{\beta\mu} + g^{\alpha\mu}g^{\beta\lambda} + \frac{2\nu}{1-\nu}g^{\alpha\beta}g^{\lambda\mu}\right), \tag{2}$$

$$D^{\alpha\lambda} = \frac{8E}{t_s^2(1+\nu)}g^{\alpha\lambda}, \tag{3}$$

where E is the Young modulus, ν the Poisson ratio, t_s the thickness and $g^{\alpha\lambda}$ the contravariant components of the metric tensor.

The MITC4 finite element has 5 degrees of freedom per node (the three components of the displacement and the two parameters which define the variation of the unit vector). This element is almost free of locking. This desirable feature is obtained by using a particular interpolation strategy for the different components of the strain tensor. We refer to [25] for more details.

2.3 Contact model

The contact is assumed to be frictionless and soft. In addition, we do not apply any specific treatment due to the presence of the fluid (no lubrication forces are added). In spite of these simplifications, the problem is quite complicated since the contact constraints are non-convex, as will be shown in the sequel.

3 General algorithm

We give in this section the details of the general algorithm which handles fluid-structure interaction and contact. We denote by M the family of immersed solids $M = (M_1, M_2, \dots)$ and by $\mathcal{T}_h$ a P_1 finite element mesh of M:

$$X = \{\boldsymbol{\varphi} \in C^0(M; \mathbb{R}^d), \boldsymbol{\varphi}|_T \in P_1, \forall T \in \mathcal{T}_h\},$$

where $d = 2$ or 3. The quantity $\boldsymbol{\varphi}(\boldsymbol{x}_i)$ is the current position of the i^{th} node of the structure. We denote by $\boldsymbol{\varphi}_\Sigma$ the restriction of $\boldsymbol{\varphi}$ to the fluid-structure interface Σ.

The structure "discrete energy" is denoted by J. The energy J includes in particular the terms resulting from the discretization of the acceleration and the load exerted by the fluid. The deformation $\boldsymbol{\varphi} : \cup_i M_i \to \mathbb{R}^d$ is determined by solving at each time step the following minimization problem:

$$\inf_{\boldsymbol{\varphi}\in\mathcal{U}} J(\boldsymbol{\varphi}), \tag{4}$$

with

$$\mathcal{U} = \{\boldsymbol{\varphi} \in X, \mathrm{dist}(\boldsymbol{\varphi}(T_1), \boldsymbol{\varphi}(T_2)) \geq \varepsilon_g, \forall T_1, T_2 \in \mathcal{T}_h \text{ such that } T_1 \cap T_2 = \emptyset\},$$

where ε_g denotes a gap between the solids. Note that the set $\mathcal{U}$ defining the constraints is non-convex which makes the minimization problem (4) difficult. This difficulty will be circumvented by transforming the problem with non-convex constraints into a sequence of problems with convex constraints.

The proposed algorithm is made of three nested loops. The external loop (loop 1) solves the fluid-structure coupling. The first inner loop (loop 2) build

a sequence of convex sets $\mathcal{C}(\boldsymbol{\varphi}^k)$ which are used in place of $\mathcal{U}$. The purpose of the most inner loop (loop 3) is to solve problem (4) on the convex sets $\mathcal{C}(\boldsymbol{\varphi}^k)$. Figure 1 summarizes this algorithm. In the three next sections, we give the details of each loop.

Loop 1: Fluid-Structure

Iterate on j until $\|\boldsymbol{\varphi}_\Sigma^{j+1} - \boldsymbol{\varphi}_\Sigma^j\| \leq \varepsilon_{fsi}$:

1. Solve the fluid problem: given the structures deformation $\boldsymbol{\varphi}_\Sigma^j$, compute the fluid velocity and pressure $(\boldsymbol{u}^j, p^j)$.

2. Compute the load exerted by the fluid $\boldsymbol{\sigma}_f^j$.

3. Loop 2: Sequence of convex minimization problems

Iterate on k until $\|\boldsymbol{\varphi}^{j,k+1} - \boldsymbol{\varphi}^{j,k}\| \leq \varepsilon_T$:

3.1. Definition of a convex neighborhood $\mathcal{C}(\boldsymbol{\varphi}^{j,k})$ of $\boldsymbol{\varphi}^{j,k}$.

3.2. Loop 3: Minimization with convex constraints

Uzawa algorithm (tolerance ε_{cvx}) to solve the structure problem:

$$J(\boldsymbol{\varphi}^{j,k+1}) = \inf J(\boldsymbol{\psi})$$

under the convex constraint $\boldsymbol{\psi} \in \mathcal{C}(\boldsymbol{\varphi}^{j,k})$.

Figure 1: General algorithm

3.1 Fluid-structure interaction (loop 1)

Several techniques have been proposed to solve the mechanical interaction between blood flow and arterial walls (among many references see *e.g.* [26, 27, 28, 29, 30, 31]). The effort to devise good coupling algorithms can be explained by the fact that naive partitioned schemes can be either unstable or very inefficient. For example, in typical configurations, an accelerated fixed point algorithm needs up to 40 iterations to converge. Explanations of this fact have been provided in [32, 33].

In the present study, we are not interested in the coupling with the wall but with an immersed valve. In this specific case, we observed that an accelerated fixed point algorithm typically converges in about 5 iterations. Thus, we adopted this simple algorithm for the fluid-valve interaction.

The acceleration of the fixed-point method is based on the Aitken formula which has been applied to FSI problems in [34]. The algorithm reads:

Loop 1 : Fluid-Structure

(i) Initial guess $\boldsymbol{\varphi}_\Sigma^0$ (prediction of the position of the interface).

(ii) For $j \geq 0$, solve the fluid problem, given an interface deformation $\boldsymbol{\varphi}_\Sigma^j$.

(iii) Compute the load $\boldsymbol{\sigma}_f^j$ exerted by the fluid on the structure.

(iv) Solve the structure to obtain a new deformation $\tilde{\boldsymbol{\varphi}}^{j+1}$.

(v) Correction of the position of the interface:

$$\boldsymbol{\varphi}_\Sigma^{j+1} = \omega^j \tilde{\boldsymbol{\varphi}}_\Sigma^{j+1} + (1-\omega^j)\boldsymbol{\varphi}_\Sigma^j,$$

with

$$\omega^j = \frac{(\boldsymbol{\varphi}_\Sigma^j - \boldsymbol{\varphi}_\Sigma^{j-1}) \cdot (\boldsymbol{\varphi}_\Sigma^j - \tilde{\boldsymbol{\varphi}}_\Sigma^{j+1} - \boldsymbol{\varphi}_\Sigma^{j-1} + \tilde{\boldsymbol{\varphi}}_\Sigma^j)}{|\boldsymbol{\varphi}_\Sigma^j - \tilde{\boldsymbol{\varphi}}_\Sigma^{j+1} - \boldsymbol{\varphi}_\Sigma^{j-1} + \tilde{\boldsymbol{\varphi}}_\Sigma^j|^2}. \tag{5}$$

(vi) While $\|\boldsymbol{\varphi}_\Sigma^{j+1} - \boldsymbol{\varphi}_\Sigma^j\| > \varepsilon_{fsi}$ go to (ii).

If the interaction with the aorta was also taken into account (which is not the case in this work), it would be necessary to use more sophisticated algorithms to avoid prohibitive computational costs. For example, the method proposed in [27] could be extended to deal with both types of interaction (wall and valve). A step in this direction is presented in [35].

3.2 Definition of a convex neighborhoods (loop 2)

Loop 2 is based on an original idea proposed in [23]. Its purpose is to replace the non-convex optimization problem (4) with a sequence of convex ones. For the sake of clarity, we drop the index j related to the FSI iteration in Figure 1. Suppose the current deformation of the structure is $\boldsymbol{\varphi}^k$. To compute the state $\boldsymbol{\varphi}^{k+1}$, we solve the structure problem (4) replacing $\mathcal{U}$ with a convex set denoted by $\mathcal{C}(\boldsymbol{\varphi}^k)$. Each convex set $\mathcal{C}(\boldsymbol{\varphi}^k)$ contains the element $\boldsymbol{\varphi}^k$ and is included in the initial admissible set $\mathcal{U}$. Moreover, if $\boldsymbol{\varphi}^k$ belongs to the interior of $\mathcal{U}$, the set $\mathcal{C}(\boldsymbol{\varphi}^k)$ is a convex (closed) neighborhood of the element $\boldsymbol{\varphi}^k$. In the following, $\mathcal{C}(\boldsymbol{\varphi}^k)$ will be often referred to a "neighborhood" of $\boldsymbol{\varphi}$ by language abuse. The precise definition of the convex neighborhood in 2D and 3D is given in the two following sections. Here is a sketch of the algorithm:

Loop 2: Sequence of convex minimization problems

(i) Initial guess: $\boldsymbol{\varphi}^0$.

(ii) For $k \geq 0$, solve

$$J(\boldsymbol{\varphi}^{k+1}) = \inf_{\boldsymbol{\psi} \in \mathcal{C}(\boldsymbol{\varphi}^k)} J(\boldsymbol{\psi}),$$

where $\mathcal{C}(\boldsymbol{\varphi}^k)$ is a convex neighborhood of $\boldsymbol{\varphi}^k$ defined below.

(iii) While $\|\boldsymbol{\varphi}^{k+1} - \boldsymbol{\varphi}^k\| > \varepsilon_{\mathcal{C}}$ go to (ii).

As $\mathcal{C}(\boldsymbol{\varphi}^k)$ always contains $\boldsymbol{\varphi}^k$, the sequence $J(\boldsymbol{\varphi}^k)$ in the loop 2 of the algorithm is non-increasing, and therefore convergent if bounded from below. The resolution of the new minimization problem (where the solution is searched in $\mathcal{C}(\boldsymbol{\varphi}^k)$) is the purpose of the third loop and will be explained later on.

Note that, at convergence, the optimality conditions of the original non-convex problem are not exactly satisfied. Nevertheless, it can be proved that they are satisfied up to an error $O(h)$, where h is the discretization step in the structure (see [23]).

3.2.1 Definition of $\mathcal{C}(\boldsymbol{\varphi}^k)$ in 2D

In 2D, the convex neighborhood is defined as follows:

$$\mathcal{C}(\boldsymbol{\psi}) = \Big\{ \boldsymbol{\varphi} \in X, \min_{\boldsymbol{x}_e \in e} \boldsymbol{n}_{e,\boldsymbol{x}}(\boldsymbol{\psi}) \cdot (\boldsymbol{\varphi}(\boldsymbol{x}_e) - \boldsymbol{\varphi}(\boldsymbol{x})) \geq \varepsilon_g, \\ \text{for all edges } e \text{ and all nodes } \boldsymbol{x} \notin e \Big\},$$

where $\varepsilon_g > 0$ and $\boldsymbol{n}_{e,\boldsymbol{x}}(\boldsymbol{\psi})$ is defined by:

$$\min_{\boldsymbol{x}_e \in e} \boldsymbol{n}_{e,\boldsymbol{x}}(\boldsymbol{\psi}) \cdot (\boldsymbol{\psi}(\boldsymbol{x}_e) - \boldsymbol{\psi}(\boldsymbol{x})) = \mathrm{dist}(\boldsymbol{\psi}(e), \boldsymbol{\psi}(\boldsymbol{x})).$$

Loosely speaking, $\boldsymbol{n}_{e,\boldsymbol{x}}(\boldsymbol{\psi})$ is the normal to the edge e pointing to the node $\boldsymbol{x}$. See Figure 2 for two typical configurations.

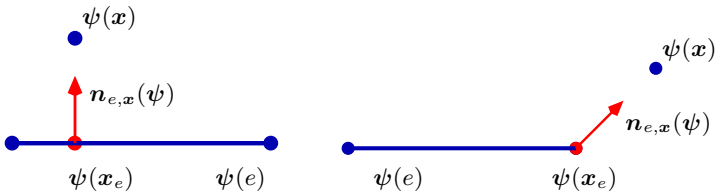

Figure 2: Definition of $\boldsymbol{n}_{e,\boldsymbol{x}}$ in two configurations.

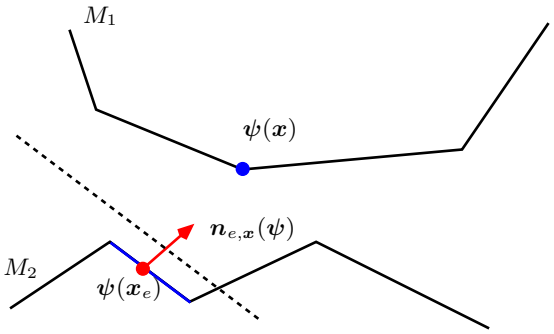

Figure 3: An example of convex constraint approximating the non-convex one: all the couples edge/vertex can be separated by a straight line (dashed-line), with a gap ε_g.

We denote by e^+ and e^- the vertices of an edge e. It is convenient to notice that the convex neighborhood can also be rewritten as:

$$\mathcal{C}(\boldsymbol{\psi}) = \Big\{ \quad \boldsymbol{\varphi} \in X, F^-_{e,\boldsymbol{x}_i}(\boldsymbol{\varphi}) \leq 0, F^+_{e,\boldsymbol{x}_i}(\boldsymbol{\varphi}) \leq 0, \\ \text{for all edges } e \text{ and all nodes } \boldsymbol{x}_i \notin e \Big\}, \tag{6}$$

where

$$F^{\pm}_{e,\boldsymbol{x}_i,\boldsymbol{\psi}}(\boldsymbol{\varphi}) = \varepsilon_g - \boldsymbol{n}_{e,\boldsymbol{x}_i}(\boldsymbol{\psi}) \cdot (\boldsymbol{\varphi}(e^{\pm}) - \boldsymbol{\varphi}(\boldsymbol{x}_i)),$$

Under this form, we see that the convex constraints consist in imposing that, after deformation, any edges and vertices can be separated by a straight line, with a gap ε_g (see Figure 3).

If loop 2 converges to $\boldsymbol{\varphi} \in X$, then there exist $\lambda^+_{e,i} \geq 0$ and $\lambda^-_{e,i} \geq 0$ (for all e and i such that node i does not belong to edge e) such that $\forall \boldsymbol{\xi} \in X$:

$$\left\{ \begin{array}{rcl} \langle J'(\boldsymbol{\varphi}), \boldsymbol{\xi} \rangle - & & \\ \displaystyle\sum_e \sum_{\boldsymbol{x}_i \notin e} \boldsymbol{n}_{e,\boldsymbol{x}_i} \cdot \left((\lambda^-_{e,\boldsymbol{x}_i} + \lambda^+_{e,\boldsymbol{x}_i}) \boldsymbol{\xi}(\boldsymbol{x}_i) - \lambda^-_{e,\boldsymbol{x}_i} \boldsymbol{\xi}(e^-) - \lambda^+_{e,\boldsymbol{x}_i} \boldsymbol{\xi}(e^+) \right) & = & 0, \\ \lambda^-_{e,\boldsymbol{x}_i} F^-_{e,\boldsymbol{x}_i,\boldsymbol{\psi}}(\boldsymbol{\varphi}) & = & 0, \\ \lambda^+_{e,\boldsymbol{x}_i} F^+_{e,\boldsymbol{x}_i,\boldsymbol{\psi}}(\boldsymbol{\varphi}) & = & 0. \end{array} \right. \tag{7}$$

The Lagrange multipliers $\lambda^{\pm}_{e,\boldsymbol{x}_i}$ represent the contact pressure acting on the nodes of the solids mesh and are added to the hydrodynamic force acting on the structure. The computation of $\lambda^{\pm}_{e,\boldsymbol{x}_i}$ will be explained in Section 3.3.

Note that self-contact is automatically handled since the non-penetration condition is tested among two generic independent elements that can also belong to the same solid.

3.2.2 Definition of $\mathcal{C}(\boldsymbol{\varphi}^k)$ in 3D

In 3D, two possible contacts can occur:

1. contacts among edges (Figure 4.a),
2. contacts among triangles and vertices (Figure 4.b).

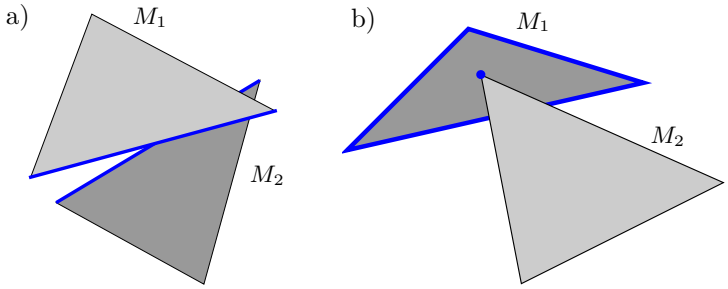

Figure 4: Possible contacts between two solids M_1 and M_2 in three-dimensions. a) Contact between two edges. b) Contact between a vertex and a triangle.

Therefore the convex neighborhood $\mathcal{C}(\boldsymbol{\varphi}^k)$ is defined as the set of admissible deformations subjected to the constraints associated to each couple edge/edge and triangle/vertex:

$$\mathcal{C}(\boldsymbol{\psi}) = \Big\{ \begin{array}{l} \boldsymbol{\varphi} \in X, \min\limits_{\boldsymbol{x}_a \in a, \boldsymbol{x}_b \in b} \boldsymbol{n}_{a,b}(\boldsymbol{\psi}) \cdot (\boldsymbol{\varphi}(\boldsymbol{x}_a) - \boldsymbol{\varphi}(\boldsymbol{x}_b)) \geq \varepsilon_g, \\ \text{for all edges } a \text{ and } b \text{ of the mesh } \mathcal{T} \text{ such that } a \cap b = \emptyset \\ \text{and } \min\limits_{\boldsymbol{x}_T \in T} \boldsymbol{n}_{T,\boldsymbol{x}}(\boldsymbol{\psi}) \cdot (\boldsymbol{\varphi}(\boldsymbol{x}_T) - \boldsymbol{\varphi}(\boldsymbol{x})) \geq \varepsilon_g, \text{for all} \\ \text{triangle } T \text{ and all vertex } \boldsymbol{x} \text{ of the mesh } \mathcal{T} \text{ such that } \boldsymbol{x} \notin T \Big\}, \end{array}$$

where $\boldsymbol{n}_{a,b}(\boldsymbol{\psi})$ and $\boldsymbol{n}_{T,\boldsymbol{x}}(\boldsymbol{\psi})$ are defined by:

$$\min_{\boldsymbol{x}_a \in a, \boldsymbol{x}_b \in b} \boldsymbol{n}_{a,b}(\boldsymbol{\psi}) \cdot (\boldsymbol{\psi}(\boldsymbol{x}_a) - \boldsymbol{\psi}(\boldsymbol{x}_b)) = \text{dist}(\boldsymbol{\psi}(a) - \boldsymbol{\psi}(b))$$

and

$$\min_{\boldsymbol{x}_T \in T} \boldsymbol{n}_{T,\boldsymbol{x}}(\boldsymbol{\psi}) \cdot (\boldsymbol{\psi}(\boldsymbol{x}_T) - \boldsymbol{\psi}(\boldsymbol{x})) = \mathrm{dist}(\boldsymbol{\psi}(T) - \boldsymbol{\psi}(\boldsymbol{x})).$$

For the sake of completeness, we now give a few details on the computations of $\boldsymbol{n}_{a,b}(\boldsymbol{\psi})$. Let us first denote by a_0, a_1 and b_0, b_1 the corresponding endpoints of the edges a and b, and by $\boldsymbol{\psi}(p_{a,b}) \in \boldsymbol{\psi}(a)$ and $\boldsymbol{\psi}(p_{b,a}) \in \boldsymbol{\psi}(b)$ the set of points that minimize the distance between $\boldsymbol{\psi}(a)$ and $\boldsymbol{\psi}(b)$ (Figure 5):

$$\begin{gathered}\boldsymbol{\psi}(p_{a,b}) = \alpha\boldsymbol{\psi}(a_0) + (1-\alpha)\boldsymbol{\psi}(a_1),\\ \boldsymbol{\psi}(p_{b,a}) = \beta\boldsymbol{\psi}(b_0) + (1-\beta)\boldsymbol{\psi}(b_1),\\ \text{with } \alpha, \beta \in \mathbb{R},\ 0 \le \alpha, \beta \le 1.\end{gathered}$$

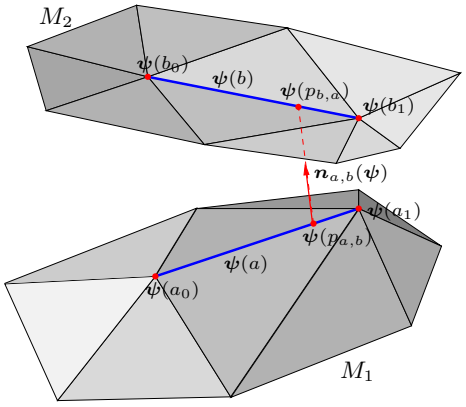

Figure 5: Computation of the unit vector $\boldsymbol{n}_{a,b}(\boldsymbol{\psi})$ for the edge/edge couple (a, b).

The coefficients α and β represent respectively the barycentric coordinates for $\boldsymbol{\psi}(p_{a,b})$ and $\boldsymbol{\psi}(p_{b,a})$ and are evaluated analytically by solving the following minimization problem:

$$(\alpha, \beta) = \operatorname*{argmin}_{0\le\alpha,\beta\le 1} f(\alpha, \beta) = \operatorname*{argmin}_{0\le\alpha,\beta\le 1} \|\boldsymbol{\psi}(p_{b,a}) - \boldsymbol{\psi}(p_{a,b})\|. \tag{8}$$

Note that problem (8) admits always a unique solution, except when $\boldsymbol{\psi}(a)$ and $\boldsymbol{\psi}(b)$ are colinear, that is when

$$\|a\|^2\|b\|^2 - (a_1 - a_0, b_1 - b_0)^2 = 0.$$

From a practical point of view it is convenient to first solve the corresponding unconstrained minimization problem and then evaluate the fulfillment of the constraints. If one of the constraints is not satisfied or if the edges are colinear, the solution of problem (8) is equivalent to

$$(\alpha, \beta) = \operatorname*{argmin}_{\alpha,\beta\in\{0,1\}} f(\alpha, \beta) = \operatorname*{argmin}_{\alpha,\beta\in\{0,1\}} \|\boldsymbol{\psi}(p_{b,a}) - \boldsymbol{\psi}(p_{a,b})\|.$$

Once the couple $(\boldsymbol{\psi}(p_{a,b}), \boldsymbol{\psi}(p_{b,a}))$ is computed, the normal vector $\boldsymbol{n}_{a,b}(\boldsymbol{\psi})$ is finally obtained by

$$\boldsymbol{n}_{a,b}(\boldsymbol{\psi}) = \frac{\boldsymbol{\psi}(p_{b,a}) - \boldsymbol{\psi}(p_{a,b})}{\|\boldsymbol{\psi}(p_{b,a}) - \boldsymbol{\psi}(p_{a,b})\|}.$$

Some possible configurations of $\boldsymbol{n}_{a,b}(\boldsymbol{\psi})$ for two generic edges a and b are presented in Figure 6.

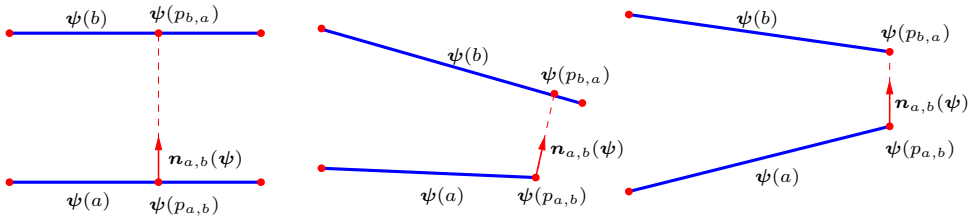

Figure 6: Possible configurations of the unit vector $\boldsymbol{n}_{a,b}(\boldsymbol{\psi})$.

Let us now consider the definition of the normal vector $\boldsymbol{n}_{T,\boldsymbol{x}}(\boldsymbol{\psi})$. In a similar way to the edge/edge contact case, we introduce the vertices (t_0, t_1, t_2) of the triangle T and the barycentric coordinates for the point $\boldsymbol{\psi}(p_{T,\boldsymbol{x}}) \in \boldsymbol{\psi}(T)$ that minimizes the distance from the vertex $\boldsymbol{\psi}(\boldsymbol{x})$ (Figure 7):

$$\boldsymbol{\psi}(p_{T,x}) = \alpha\boldsymbol{\psi}(t_0) + \beta\boldsymbol{\psi}(t_1) + (1-\alpha-\beta)\boldsymbol{\psi}(t_2),$$
$$\text{with } \alpha, \beta, \gamma \in \mathbb{R},\ 0 \leq \alpha, \beta, \gamma \leq 1 \text{ and } \gamma = 1-\alpha-\beta.$$

The coefficients α, β and γ are determined by

$$(\alpha, \beta) = \underset{\substack{0\leq\alpha,\beta,\gamma\leq 1\\ \gamma=1-\alpha-\beta}}{\operatorname{argmin}}\ g(\alpha,\beta) = \underset{\substack{0\leq\alpha,\beta,\gamma\leq 1\\ \gamma=1-\alpha-\beta}}{\operatorname{argmin}}\ \|\boldsymbol{\psi}(p_{T,\boldsymbol{x}}) - \boldsymbol{\psi}(\boldsymbol{x})\|, \tag{9}$$

and $\boldsymbol{n}_{T,\boldsymbol{x}}(\boldsymbol{\psi})$ is obtained from:

$$\boldsymbol{n}_{T,\boldsymbol{x}}(\boldsymbol{\psi}) = \frac{\boldsymbol{\psi}(p_{T,\boldsymbol{x}}) - \boldsymbol{\psi}(\boldsymbol{x})}{\|\boldsymbol{\psi}(p_{T,\boldsymbol{x}}) - \boldsymbol{\psi}(\boldsymbol{x})\|}.$$

From a computational point of view, instead of solving directly the constrained

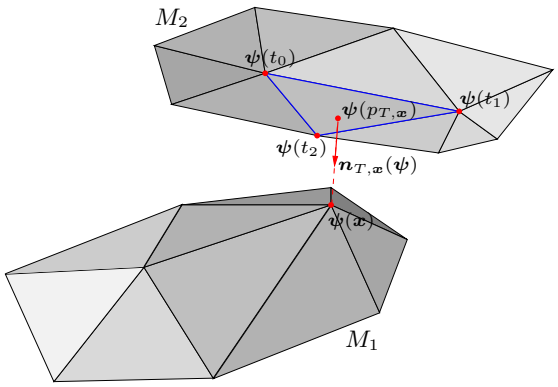

Figure 7: Computation of the unit vector $\boldsymbol{n}_{T,\boldsymbol{x}}(\boldsymbol{\psi})$ for the triangle/vertex couple $(T, \boldsymbol{x})$.

problem (9), it is easier to determine first the relative position of the point $\boldsymbol{\psi}(\boldsymbol{x})$ with respect to $\boldsymbol{\psi}(T)$ and then solve a subproblem to calculate $\boldsymbol{\psi}(p_{T,\boldsymbol{x}})$.

In particular, considering the triangle in Figure 8.a, $\boldsymbol{\psi}(p_{T,\boldsymbol{x}})$ will be computed as the projection of $\boldsymbol{\psi}(\boldsymbol{x})$ on the edge $\boldsymbol{\psi}(e_i)$ $(\forall i \in \{0,1,2\})$ if $\boldsymbol{\psi}(\boldsymbol{x})$ is in the part of the space opposed to $\boldsymbol{\psi}(t_i)$ with respect to the plane perpendicular to $\boldsymbol{\psi}(T)$ that contains $\boldsymbol{\psi}(e_i)$. Therefore, in this case, the triangle/vertex problem is equivalent to an edge/vertex problem in three-dimensions. On the other hand (Figure 8.b), if $\boldsymbol{\psi}(\boldsymbol{x})$ belongs to the cylinder determined by the intersection of the three perpendicular planes previously defined, $\boldsymbol{\psi}(p_{T,\boldsymbol{x}})$ will be determined by the analytical solution of the unconstrained problem

$$(\alpha,\beta) = \operatorname{argmin} g(\alpha,\beta) = \operatorname{argmin} \|\boldsymbol{\psi}(p_{T,\boldsymbol{x}}) - \boldsymbol{\psi}(\boldsymbol{x})\|,$$

which is equivalent to the projection of the vertex $\boldsymbol{\psi}(\boldsymbol{x})$ on the infinite plane defined by (t_0,t_1,t_2).

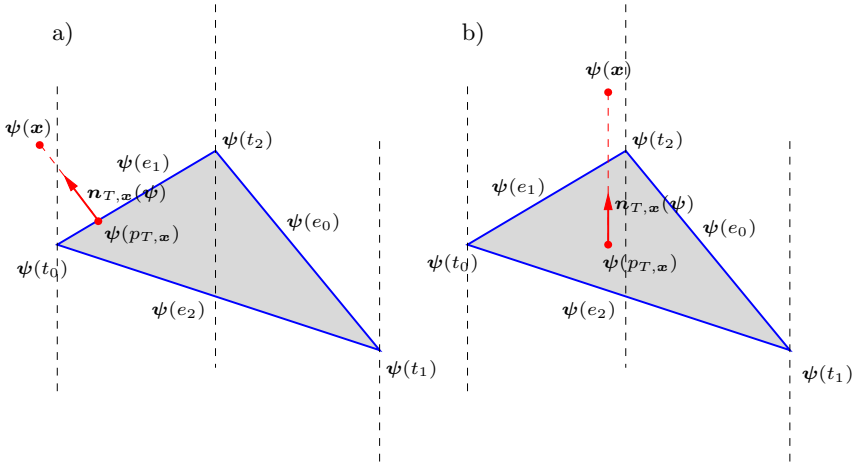

Figure 8: Possible configurations of the unit vector $\boldsymbol{n}_{T,\boldsymbol{x}}(\boldsymbol{\psi})$. a) $\boldsymbol{\psi}(\boldsymbol{x})$ is in the part of the space opposed to $\boldsymbol{\psi}(t_1)$ with respect to the plane that contains $\boldsymbol{\psi}(e_1)$. b) $\boldsymbol{\psi}(\boldsymbol{x})$ is inside the cylinder determined by the intersection of the three perpendicular planes to $\boldsymbol{\psi}(T)$.

As in the bidimensional case, we can note that the convex neighborhood can also be rewritten as:

$$\mathcal{C}(\boldsymbol{\psi}) = \Big\{ \begin{array}{l} \boldsymbol{\varphi} \in X, F^{j,k}_{a,b}(\boldsymbol{\varphi}) \leq 0 \ \forall j,k \in \{0,1\}, \\ \text{for all edges } a \text{ and } b \text{ of the mesh } \mathcal{T} \text{ such that } a \cap b = \emptyset \\ \text{and } F^{k}_{T,\boldsymbol{x}_i}(\boldsymbol{\varphi}) \leq 0 \ \forall k \in \{0,1,2\}, \text{for all triangle } T \\ \text{and all vertex } x \text{ of the mesh } \mathcal{T} \text{ such that } x \notin T \Big\}, \end{array} \tag{10}$$

where

$$F^{j,k}_{a,b,\boldsymbol{\psi}}(\boldsymbol{\varphi}) = \varepsilon_g - \boldsymbol{n}_{a,b}(\boldsymbol{\psi}) \cdot (\boldsymbol{\varphi}(a_j) - \boldsymbol{\varphi}(b_k)),$$

and

$$F^{k}_{T,\boldsymbol{x}_i,\boldsymbol{\psi}}(\boldsymbol{\varphi}) = \varepsilon_g - \boldsymbol{n}_{T,\boldsymbol{x}_i}(\boldsymbol{\psi}) \cdot (\boldsymbol{\varphi}(t_k) - \boldsymbol{\varphi}(\boldsymbol{x}_i)).$$

If loop 2 converges, the limit satisfies the following optimality system:

$$\left\{\begin{array}{rcl} \langle J'(\boldsymbol{\varphi}),\boldsymbol{\xi}\rangle & - & \displaystyle\sum_a \sum_{\substack{b\\ a\cap b=\emptyset}} \boldsymbol{n}_{T,\boldsymbol{x}_i}\cdot\big(\sum_{j=0}^{2}\sum_{k=0}^{2}\lambda_{a,b}^{j,k}\boldsymbol{\xi}(a_j)-\lambda_{a,b}^{j,k}\boldsymbol{\xi}(b_k)\big) \\ & - & \displaystyle\sum_T \sum_{\boldsymbol{x}_i\notin T} \boldsymbol{n}_{T,\boldsymbol{x}_i}\cdot\big(\sum_{k=0}^{3}\lambda_{T,\boldsymbol{x}_i}^{k}\boldsymbol{\xi}(\boldsymbol{x}_i)-\lambda_{T,\boldsymbol{x}_i}^{k}\boldsymbol{\xi}(t_k)\big)=0 \qquad \forall\boldsymbol{\xi}\in X, \\ & & \lambda_{a,b}^{j,k}F_{a,b,\boldsymbol{\psi}}^{j,k}(\boldsymbol{\varphi})=0 \qquad \forall j,k\in\{0,1\}, \\ & & \lambda_{T,\boldsymbol{x}_i}^{k}F_{T,\boldsymbol{x}_i,\boldsymbol{\psi}}^{k}(\boldsymbol{\varphi})=0 \qquad \forall k\in\{0,1,2\}. \end{array}\right. \tag{11}$$

where $\lambda_{a,b}^{j,k}\geq 0$ and $\lambda_{T,\boldsymbol{x}}^{k}\geq 0$ represent respectively the four Lagrange multipliers associated to the (a,b) edge/edge problem and the three ones associated to the $(T,\boldsymbol{x}_i)$ triangle/vertex problem.

3.3 Minimization with convex constraints (loop 3)

The most inner loop aims at solving an optimization problem with convex constraints: given an hydrodynamic force $\boldsymbol{\sigma}_f^j$ (loop 1), given a convex neighborhood $\mathcal{C}(\boldsymbol{\psi})$ of the current solid deformation $\boldsymbol{\psi}=\boldsymbol{\varphi}^{j,k}$ (loop 2), we have to solve

$$\inf_{\boldsymbol{\varphi}\in\mathcal{C}(\boldsymbol{\psi})} J(\boldsymbol{\varphi}), \tag{12}$$

The convex set $\mathcal{C}(\boldsymbol{\psi})$ being defined by (6) in 2D and by (10) in 3D.

To solve problem (12), various methods – like penalization or relaxation with projection – may yield substantial changes of the structure solver. Here we adopt a method which consists in maximizing a dual energy. We present it in 2D, the extension in 3D being obtained *mutatis mutandis*.

Denoting by μ the vector $(\mu_{e,\boldsymbol{x}_i}^{\pm})$, where $(e,\boldsymbol{x}_i)$ describes all the couples edge/nodes such that $\boldsymbol{x}_i\notin e$, we look for the maximum of the dual energy

$$G(\mu)=\inf_{\boldsymbol{\varphi}\in X}\left[J(\boldsymbol{\varphi})+\sum_e\sum_{\boldsymbol{x}_i\notin e}\big(\mu_{e,\boldsymbol{x}_i}^{-}F_{e,\boldsymbol{x}_i,\boldsymbol{\psi}}^{-}(\boldsymbol{\varphi})+\mu_{e,\boldsymbol{x}_i}^{+}F_{e,\boldsymbol{x}_i,\boldsymbol{\psi}}^{+}(\boldsymbol{\varphi})\big)\right],$$

under the constraint $\mu_{e,\boldsymbol{x}_i}^{\pm}\geq 0$. In a gradient method with projection, these constraints are very easy to implement, whereas the original one, namely $\boldsymbol{\varphi}\in\mathcal{C}(\boldsymbol{\psi})$, is complicated. This is the usual motivation of the dual approach. In our specific framework, this method has another advantage: during the resolution by a gradient method of the dual problem, the structure solver exchanges the same kind of information as for the coupling with the fluid (it receives loads, it sends displacements, see Figure 9). The contact treatment can therefore be easily included as an inner-loop in the global algorithm without any change in the structure solvers. Even if other optimization methods are known to perform better than the gradient method, the possibility to use the structure solver as a "black-box" is a strong motivation for the proposed approach.

We can sum up the loop 3 as follows:

(i) Initial guess: λ^0.

(ii) Solve the structure problem: find $\boldsymbol{\varphi}^l \in X$ such that for all $\boldsymbol{\xi} \in X$,

$$\langle J'(\boldsymbol{\varphi}^l), \boldsymbol{\xi} \rangle = -\sum_e \sum_{\boldsymbol{x}_i \notin e} \lambda^-_{e,\boldsymbol{x}_i} \langle (F^-_{e,\boldsymbol{x}_i,\boldsymbol{\psi}})'(\boldsymbol{\varphi}^l), \boldsymbol{\xi} \rangle + \lambda^+_{e,\boldsymbol{x}_i} \langle (F^+_{e,\boldsymbol{x}_i,\boldsymbol{\psi}})'(\boldsymbol{\varphi}^l), \boldsymbol{\xi} \rangle$$
$$= \sum_e \sum_{\boldsymbol{x}_i \notin e} \boldsymbol{n}_{e,\boldsymbol{x}_i}(\psi) \cdot \big((\lambda^-_{e,\boldsymbol{x}_i} + \lambda^+_{e,\boldsymbol{x}_i}) \boldsymbol{\xi}(\boldsymbol{x}_i) - \lambda^-_{e,\boldsymbol{x}_i} \boldsymbol{\xi}(e^-) - \lambda^+_{e,\boldsymbol{x}_i} \boldsymbol{\xi}(e^+) \big).$$

(iii) Gradient iteration with projection:

$$\lambda^{l+1,\pm}_{e,\boldsymbol{x}_i} = \mathbf{P}_{\mathbb{R}^+} \left(\lambda^{l,\pm}_{e,\boldsymbol{x}_i} + \alpha^l F^{\pm}_{e,\boldsymbol{x}_i}(\boldsymbol{\varphi}^l) \right).$$

(iv) Go to (ii) until convergence.

The projection operator introduced in step (iii) is defined by:

$$\mathbf{P}_{\mathbb{R}^+}(x) = \begin{cases} x & \text{if} \quad x > 0 \\ 0 & \text{if} \quad x \leq 0 \end{cases}$$

Remark 1 *For efficiency, it is of course recommended to restrict the sets edge/vertex in 2D or edge/edge, triangle/vertex in 3D to those elements which can actually experience contact.*

Remark 2 [chordae tendineae] *Contacts are not the only relevant constraints in the applications to cardiac valves. For example, the* chordae tendineae *prevent the leaflet of the mitral valves from everting into the atrium. We have also implemented the capability to deal with such constraints in our framework. More precisely, let C be a point on the ventricular wall, and let M be the point of the valve to which a* chorda *(length L) is attached. It is straightforward to adapt the dual algorithm presented above to the constraint:*

$$dist(C, M) \leq L.$$

The Lagrange multiplier corresponds in this case to the tension applied on the valve by the string. Once again, the structure codes have not been modified which is an additional illustration of the versatility of the method.

3.4 Remarks on implementation

The independent solvers are coupled by exchanging "messages" (through PVM or MPI). The organization is sketched in Figure 9: a "fluid-structure master" manages the FSI coupling algorithm (loop 1), while a "structure master" manages the contact (loop 2 and 3). Whatever the coupling algorithm (loosely coupled, strongly coupled, *etc.*), whatever the fluid formulation (ALE, fictitious domains, or both), whatever the number and the kind of structures (valves, walls), in presence of contact or not, the only modification to perform in existing solvers are as limited as possible: for the fluid, it only consists in sending a load and receiving displacements whereas, for the structure it only consists in sending displacements and receiving a load.

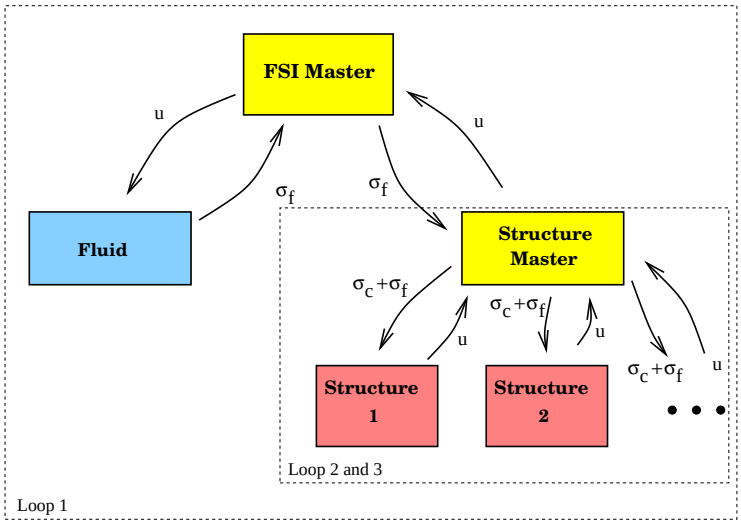

Figure 9: FSI with multi-body contacts: σ_f stands for hydrodynamic force, and σ_c for the contact force.

4 Numerical experiments

In this section we present some numerical results obtained on a realistic geometry of an aortic valve with the aim of testing the proposed algorithm.

The aortic valve lets the blood flowing in the ascending aorta, and prevents its back flow to the heart. It is composed of three semilunar leaflets attached to the aortic root. Behind them, three anatomic dilatations define the Valsalva sinuses in which the two coronary arteries are attached. A bidimensional sketch of the valve is presented in Figure 10. Some anatomical characteristics and mechanical properties of the valve can be found in [8, 36].

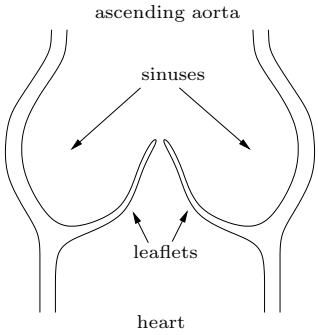

Figure 10: Bidimensional representation of the aortic valve.

Since the target of the numerical simulation is to test the multi-body contact algorithm, only the leaflet of the valve are considered flexible (red colored in Figure 11); the remaining part, blue colored, is the fluid domain boundary, Γ_{wall}, which is fixed. For a more realistic simulation also the fluid-structure interaction between the aorta wall and the blood has to be taken into account.

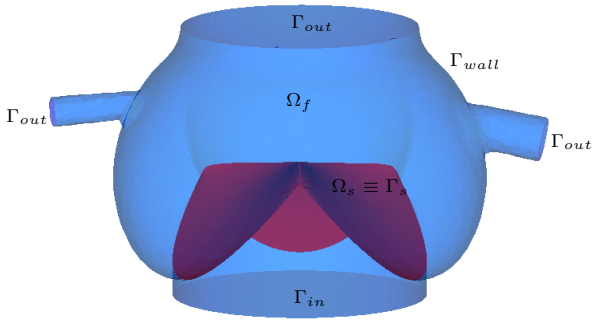

Figure 11: Computational domain.

The discretized domain contains approximately 80000 tetrahedra for the fluid (Figure 12) and 2500 shell elements for the solid (Figure 13).

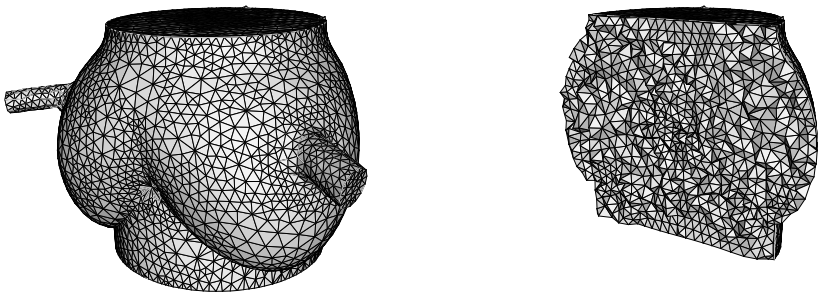

Figure 12: Fluid computational domain. On the left: surface mesh. On the right: inside clipping to show the spatial discretization step.

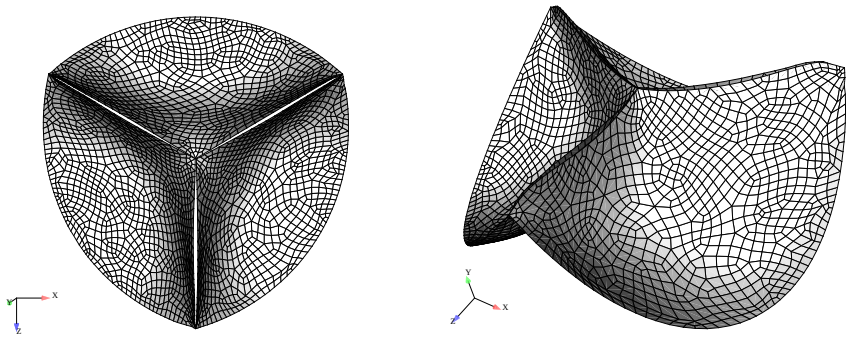

Figure 13: Structure computational domain from two different viewpoints.

From the mathematical viewpoint, the issue of contacts between bodies immersed in a viscous fluid is complicated and can lead to paradoxical results. For example, it is proved in [37] that an immersed body cannot reach in finite time the boundary of the cavity surrounding the fluid. This interesting problem is

beyond the scope of this paper. From the computational viewpoint, it clearly appears that contacts do occur and have to be handled. To illustrate this point, we propose two simulations: the first one without handling the contact, the second one handling it with the contact algorithm proposed above.

We provide here the details of the test case. A periodic pressure difference is applied between the inlet and outlet of the fluid domain. On Γ_{in} the following pressure function is imposed:

$$p_{in} = \begin{cases} A & \text{if} \quad 0 \leq t \leq \frac{13T}{28} \\ -A & \text{if} \quad \frac{13T}{28} \leq t \leq T \end{cases},$$

with amplitude $A = 130\, dyne\, cm^{-2}$ and period $T = 0.28\, s$. Note that the duration of the systolic phase roughly corresponds to the physiological one. But, in order to test the robustness of the algorithm over several opening and closure cycles, we have artificially reduced the duration of the diastole. On Γ_{out} free boundary conditions are set: $p_{out} = 0$; while on Γ_{wall} and Γ_s no slip boundary conditions are imposed. For the fluid, the density ρ_f and the dynamic viscosity μ_f are respectively $1.0\, g\, cm^{-2}$ and $0.03\, poise$. For the solid, a valve thickness of $0.65\, mm$ has been considered. The structure density ρ_s and the Young modulus E are respectively $1.2\, g\, cm^{-2}$ and $10000\, dyne/cm^2$. Both the simulations run with a timestep Δt of $10^{-3}\, s$ for a total time of $3T$ to attend the periodic condition; the fluid-structure tolerance ε_{fsi} is finally set to 10^{-4}. For the contact algorithm a gap of $10^{-3}\, cm$ is imposed and the tolerances $\varepsilon_{\mathcal{C}}$ and ε_{cvx} are respectively fixed to $5.\ 10^{-6}$ and $5.\ 10^{-7}$.

At the closure of the valve, if the contact is not handled, a non-physical overlap of the leaflets is observed, as illustrated in Figure 14. This of course results in a dramatic change of the flow and the structure displacements. Moreover, in this case, locking phenomena among the leaflets or numerical instabilities can also happen, as noticed in [35]. These observations confirm the importance of correctly manage the contact.

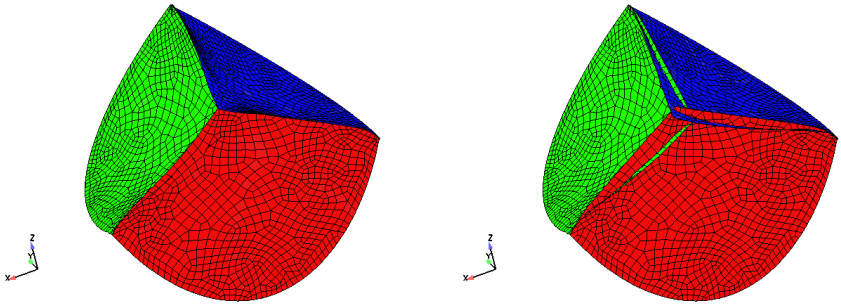

Figure 14: Comparison between the two simulations at $t = 0.259\, s$. On the left side, the contact among leaflets is handled with the contact algorithm, on the right side, it isn't.

In Figures 15 and 16, the valve displacements, the blood velocity and pressure are reported for different timesteps in the case of contact handling. A maximum velocity of approximatively $20\, cm/s$ has been obtained during the simulation. At timesteps 0.212 and 0.268, the velocity vectors show in partic-

ular the blood recirculations that happen behind the aortic valve. Moreover, a pressure jump across the valve could be observed during the closure period.

5 Conclusion

We have presented a partitioned strategy to solve fluid-structure interaction problems in which contacts among different deformable bodies can occur. A possible application of this partitioned strategy is the movements of thin valves immersed in an incompressible viscous fluid.

The proposed scheme is conceived to address the problem with existing structure solvers that are not supposed to handle contact by themselves. The non-convex constraint optimization problem defined by the hypothesis of non-penetration among solid objects is solved with an iterative algorithm which solves a series of convex constraint optimization problem. The bidimensional and tridimensional formulations are introduced and some details of the implementation are given.

A simulation of an idealized aortic valve is presented with the purpose of illustrating the algorithm in a non trivial configuration. In the proposed test case, several simplifications have been done, in particular the aortic root has been assumed to be fixed. More realistic physiological conditions will be investigated in future works.

6 Acknowledgments

This work has been partially supported by the CardioSense3D action (INRIA) and by a grant from Région Ile-de-France.

We are debtful to Marc Thiriet and Tran Tan for the mesh of the aortic root.

References

[1] E. Weinberg, M. Kaazempur-Mofrad, On the constitutive models for heart valve leaflet mechanics, Cardiovasc Engng. 5 (1) (2005) 37–43.

[2] J. de Hart, F. Baaijens, G. Peters, P. Schreurs, A computational fluid-structure interaction analysis of a fiber-reinforced stentless aortic valve, J. Biomech. 36 (2003) 699–712.

[3] E. Weinberg, M. Kaazempur-Mofrad, Transient, three-dimensional, multi-scale simulations of the human aortic valve, DOI 10.1007/s10558-007-9038-4 (2007).

[4] B. E. Griffith, R. D. Hornung, D. M. McQueen, C. S. Peskin, An adaptive, formally second order accurate version of the immersed boundary method, J. Comput. Phys. 223 (1) (2007) 10–49.

[5] Z. Jianhai, C. Dapeng, Z. Shengquan, ALE finite element analysis of the opening and closing process of the artificial mechanical valve, Appl. Math. and Mech. 17 (5) (1996) 403–412.

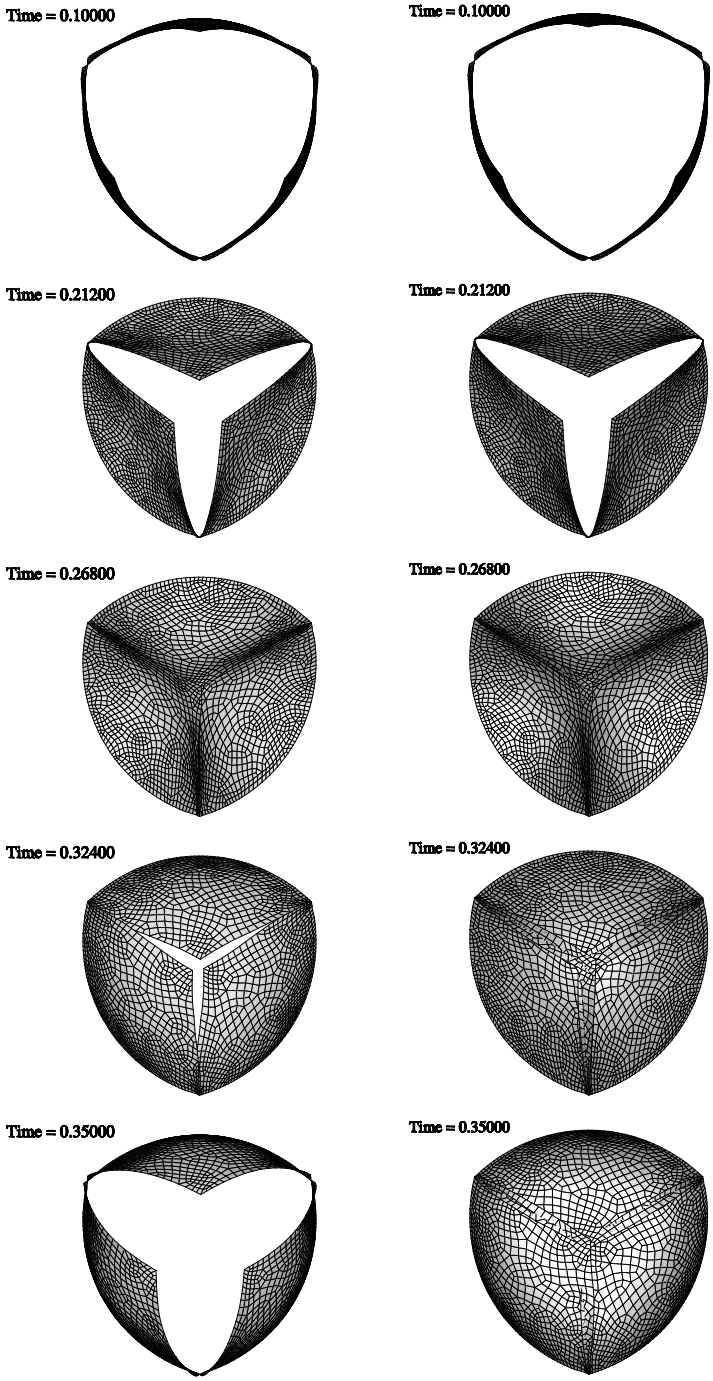

Figure 15: Valve displacements for five different timesteps in the simulations with (left) and without (right) contact handling. Note the dramatic difference between them at the reopening of the valve.

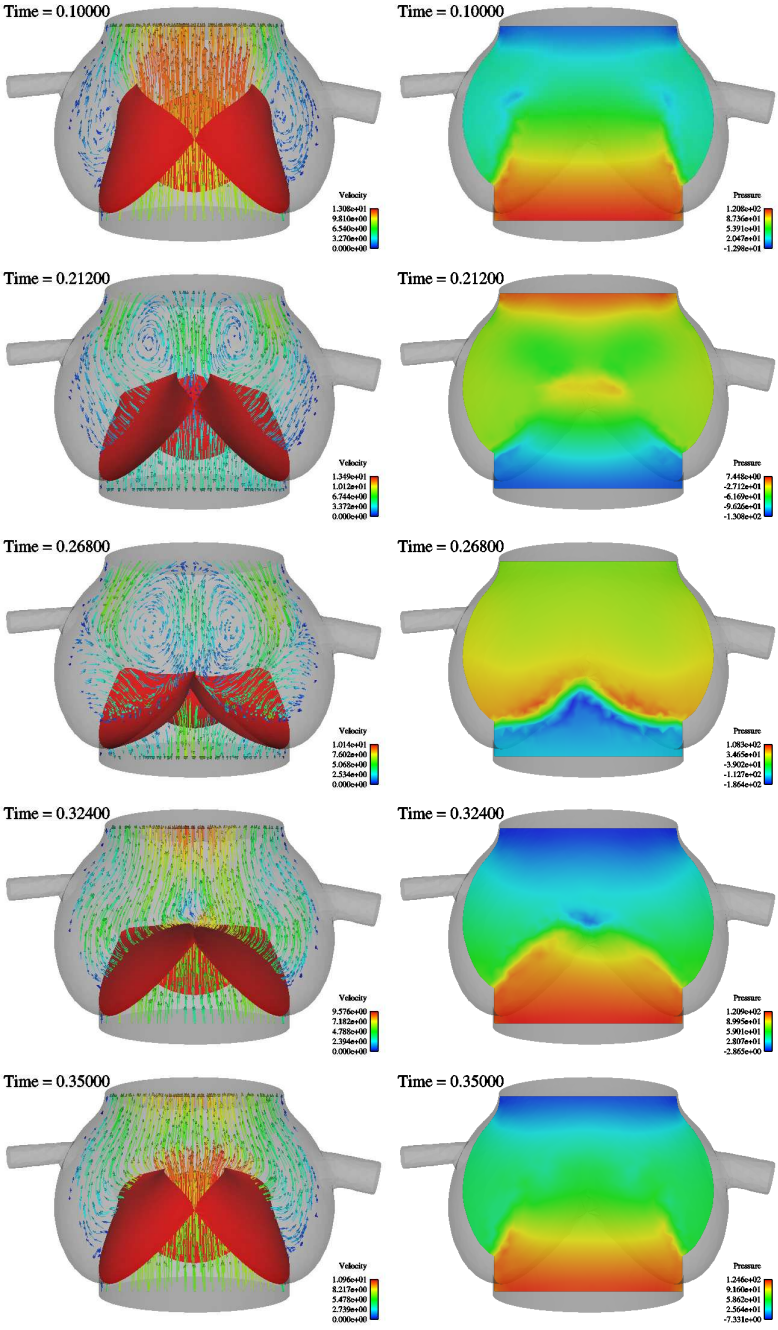

Figure 16: Blood velocity vectors (left) and pressure field (right) for 5 different timesteps.

[6] Y. Morsi, W. Yang, C. Wong, S. Das, Transient fluid-structure coupling for simulation of a trileaflet heart valve using weak coupling, J. Artif. Organs 10 (2007) 96–103.

[7] F. Baaijens, A fictitious domain/mortar element method for fluid-structure interaction, Int. J. Num. Meth. Fluids 35 (2001) 743–761.

[8] J. de Hart, G. Peters, P. Schreurs, F. Baaijens, A three-dimensional computational analysis of fluid-structure interaction in the aortic valve, J. Biomech. 36 (2003) 103–112.

[9] J. de Hart, Evaluation of a fictitious domain method for predicting dynamic response of mechanical heart valves, Journal of Fluids and Structures 19 (2004) 835–850.

[10] N. M. Diniz Dos Santos, J.-F. Gerbeau, J.-F. Bourgat, A partitioned fluid-structure algorithm for elastic thin valves with contact, comp. Meth. Appl. Mech. Engng., available online, april 2007.

[11] T. A. Laursen, Formulation and treatment of frictional contact problems using finite elements, SUDAM Report 92 (6).

[12] T. A. Laursen, Computational contact and impact mechanics. Fundamentals of modeling interfacial phenomena in nonlinear finite element analysis, Springer-Verlag, Berlin, 2002.

[13] T. A. Laursen, J. C. Simo, A continuum-based finite element formulation for the implicit solution of multibody, large deformation frictional contact problems., Internat. J. Numer. Methods Engrg. 36 (20) (1993) 3451–3485.

[14] M. W. Heinstein, S. W. Attaway, J. W. Swegle, F. J. Mello, A general-purpose contact detection algorithm for nonlinear structural analysis code, Sandia Report, 1993.

[15] J. O. Hallquist, G. L. Goudreau, D. J. Benson, Sliding interfaces with contact-impact in large-scale Lagrangian computations, Comput. Methods Appl. Mech. Engrg. 51 (1-3) (1985) 107–137, FENOMECH '84, Part I, II (Stuttgart, 1984).

[16] N. Kikuchi, J. T. Oden, Contact problems in elasticity: a study of variational inequalities and finite element methods, Vol. 8 of SIAM Studies in Applied Mathematics, Society for Industrial and Applied Mathematics (SIAM), Philadelphia, PA, 1988.

[17] P. Wriggers, Computational Contact Mechanics, J. Wiley & Sons, New York, 2002.

[18] P. Wriggers, Finite element algorithms for contact problems, Arch. Comput. Methods Engrg. 2 (4) (1995) 1–49.

[19] A. Klarbring, Large displacement frictional contact: a continuum framework for finite element discretization, European J. Mech. A Solids 14 (2) (1995) 237–253.

[20] R. van Loon, P. Anderson, F. van de Vosse, A fluid-structure interaction method with solid-rigid contact for heart valve dynamics, J. Comp. Phys. 217 (2006) 806–823.

[21] C. Carmody, G. Burriesci, I. Howard, E. Patterson, An approach to the simulation of fluid-structure interaction in the aortic valve, J. Biomech. 39 (2006) 158–169.

[22] T. E. Tezduyar, S. Sathe, Modeling of Fluid-Structure Interactions with the Space-Time Finite Elements: Solution Techniques, Internat. J. Numer. Methods Fluids 54 (2007) 855–900.

[23] O. Pantz, A frictionless contact algorithm for deformable bodies, preprint available.

[24] D. Chapelle, K. Bathe, The Finite Element Analysis of Shells - Fundamentals, Springer Verlag, 2003.

[25] K. Bathe, Finite Element Procedures, Prentice Hall, 1996.

[26] J.-F. Gerbeau, M. Vidrascu, A quasi-Newton algorithm based on a reduced model for fluid-structure interactions problems in blood flows, Math. Model. Num. Anal. 37 (4) (2003) 631–648.

[27] M. Fernández, J.-F. Gerbeau, C. Grandmont, A projection semi-implicit scheme for the coupling of an elastic structure with an incompressible fluid, Int. J. Num. Meth. Engng. 69 (2006) 794–821.

[28] M. Fernández, M. Moubachir, A Newton method using exact Jacobians for solving fluid-structure coupling, Comp. & Struct. 83 (2005) 127–142.

[29] S. Badia, F. Nobile, C. Vergara, Fluid-structure partitioned procedures based on Robin transmission conditions, Tech. Rep. 04, MOX (2007).

[30] R. Torii, M. Oshima, T. Kobayashi, K. Takagi, T. E. Tezduyar, Computer Modeling of Cardiovascular Fluid-Structure Interactions with the Deforming-Spatial-Domain/Stabilized Space-Time Formulation, Comput. Methods Appl. Mech. Engrg. 70 (2006) 1885–1895.

[31] C. Figueroa, I. Vignon-Clementel, K. Jansen, T. Hughes, C. Taylor, A coupled momentum method for modeling blood flow in three-dimensional deformable arteries, Computer Methods in Applied Mechanics and Engineering 195 (2006) 5685–5706.

[32] P. Causin, J.-F. Gerbeau, F. Nobile, Added-mass effect in the design of partitioned algorithms for fluid-structure problems, Comput. Methods Appl. Mech. Engrg. 194 (42-44) (2005) 4506–4527.

[33] C. Förster, W. Wall, E. Ramm, Artificial added mass instabilities in sequential staggered coupling of nonlinear structures and incompressible flows, Comp. Meth. Appl. Mech. Engrg. 196 (2006) 1278–1293.

[34] D. Mok, W. Wall, E. Ramm, Accelerated iterative substructuring schemes for instationary fluid-structure interaction, in: K. Bathe (Ed.), Computational Fluid and Solid Mechanics, Elsevier, 2001, pp. 1325–1328.

[35] N. Diniz Dos Santos, Numerical methods for fluid-structure interaction problems with valves, PhD Thesis, Université Pierre et Marie Curie, Paris 6.

[36] M. Thiriet, Biology and Mechanics of Blood Flows, part II: Mechanics and Medical Aspects of Blood Flows, Springer, New York, 2008.

[37] M. Hillairet, Lack of collision between solid bodies in a 2D incompressible viscous flow, to appear in Communication in Partial Differential Equations.

Centre de recherche INRIA Paris – Rocquencourt
Domaine de Voluceau - Rocquencourt - BP 105 - 78153 Le Chesnay Cedex (France)

Centre de recherche INRIA Bordeaux – Sud Ouest : Domaine Universitaire - 351, cours de la Libération - 33405 Talence Cedex
Centre de recherche INRIA Grenoble – Rhône-Alpes : 655, avenue de l'Europe - 38334 Montbonnot Saint-Ismier
Centre de recherche INRIA Lille – Nord Europe : Parc Scientifique de la Haute Borne - 40, avenue Halley - 59650 Villeneuve d'Ascq
Centre de recherche INRIA Nancy – Grand Est : LORIA, Technopôle de Nancy-Brabois - Campus scientifique
615, rue du Jardin Botanique - BP 101 - 54602 Villers-lès-Nancy Cedex
Centre de recherche INRIA Rennes – Bretagne Atlantique : IRISA, Campus universitaire de Beaulieu - 35042 Rennes Cedex
Centre de recherche INRIA Saclay – Île-de-France : Parc Orsay Université - ZAC des Vignes : 4, rue Jacques Monod - 91893 Orsay Cedex
Centre de recherche INRIA Sophia Antipolis – Méditerranée : 2004, route des Lucioles - BP 93 - 06902 Sophia Antipolis Cedex

Éditeur
INRIA - Domaine de Voluceau - Rocquencourt, BP 105 - 78153 Le Chesnay Cedex (France)
http://www.inria.fr
ISSN 0249-6399